Solid State Phenomena
ISSN: 1662-9779, Vol. 390, pp 97-109
doi:10.4028/p-cF5aLT

Submitted: 2026-01-18
Revised: 2026-02-18
Accepted: 2026-02-21
Online: 2026-04-17

Quantifying Grain Boundary and Orientation Effects on Copper under Compression: A Crystal Plasticity Finite Element Approach

PAÇACI, M. Batuhan[1,a*], DARENDELİLER Haluk[1,b]

[1]Department of Mechanical Engineering, Middle East Technical University, 06800 Ankara Türkiye

[a]pacaci.batuhan@metu.edu.tr, [b]hdarende@metu.edu.tr

Keywords: Crystal Plasticity, Grain Size, Grain Boundary, Simple Compression

Abstract. The plastic deformation behavior of polycrystalline copper is strongly governed by microstructural attributes such as grain boundaries and crystallographic orientation. While previous studies have examined microstructural features such as grain size and crystallographic orientation, these factors are often treated as isolated [1,2]. In this study, the individual and coupled effects of grain size and orientation distribution on the mechanical response of copper are investigated using the crystal plasticity finite element method. Uniaxial compression simulations are performed employing an Abaqus user-material subroutine (UMAT) subroutine, and the resulting stress–strain response, slip system activity, and strain localization are examined. Polycrystalline representative volume elements (RVEs) with varying grain sizes and textures are generated to quantify their influence on flow behavior and dislocation density. The results indicate that grain refinement diminishes orientation sensitivity and the influence of individual grains, while enhancing material strength. Moreover, grain boundaries promote heterogeneous slip, localized deformation near grain edges, and increased stress–strain heterogeneity.

Introduction

The plastic deformation of polycrystalline metals arises from crystallographic slip and its interaction with microstructural features such as grain size, grain boundaries, and orientation distribution. Classical continuum plasticity models, although computationally efficient, rely on homogenized material descriptions and therefore fail to capture orientation-dependent anisotropy, strain localization, and intergranular heterogeneity observed experimentally [3].

Crystal Plasticity theory provides a physically motivated framework by linking macroscopic deformation to slip-system-level kinematics and hardening mechanisms [4]. Early constitutive formulations established the theoretical foundation for crystal plasticity by explicitly incorporating resolved shear stress–based slip activation and finite deformation kinematics [5]. Subsequent numerical implementations enabled the integration of crystal plasticity into finite element frameworks, allowing grain-scale stress–strain heterogeneity and texture evolution to be resolved explicitly [6].

Dislocation-based theories first introduced the concept of geometrically necessary dislocations (GNDs) as a mechanistic link between lattice incompatibility and continuum-scale fields, providing a theoretical basis for capturing deformation-induced lattice curvature [7]. Subsequent experimental observations revealed pronounced strain localization and lattice curvature accumulation in the vicinity of grain boundaries, confirming their active role in governing deformation heterogeneity [8, 9]. Building on this theoretical–experimental foundation, crystal plasticity finite element formulations enabled a more comprehensive representation of grain-scale plastic deformation [10].

The increasing demand for micro- and nano-scale material characterization, together with the steady growth in computational power and simulation capability over recent decades, has enabled the investigation of material behavior at progressively smaller length scales. Within this context, the Crystal Plasticity Finite Element Method (CPFEM) has emerged as a robust framework for linking microstructural features to macroscopic mechanical response in polycrystalline metals. In this study, the effects of grain size, crystallographic orientation variation, and their coupled outcomes on the plastic deformation of polycrystalline copper are systematically investigated using CPFEM.

Representative Volume Elements (RVEs) with prescribed microstructural characteristics are generated, and uniaxial compression simulations are performed to evaluate macroscopic stress–strain response, slip activity, and strain localization. The results provide micromechanical insight into how microstructural topology governs deformation behavior in Face-Centered-Cubic (FCC) metals, contributing to improved microstructure-sensitive predictive modeling.

Governing Equations and Modeling

Crystal plasticity is formulated within a finite deformation framework, where the deformation gradient, $\boldsymbol{F}$, is multiplicatively decomposed into elastic and plastic parts as $\boldsymbol{F}^*$ and $\boldsymbol{F}^p$, respectively. The velocity gradient $\boldsymbol{L}$ is defined as

$$\boldsymbol{L} = \dot{\boldsymbol{F}}^* \cdot \boldsymbol{F}^{*-1} + \boldsymbol{F}^* \cdot \dot{\boldsymbol{F}}^P \cdot \boldsymbol{F}^{P^{-1}} \cdot \boldsymbol{F}^{*-1}. \quad (1)$$

The plastic part of velocity gradient is expressed as a sum over all slip systems

$$\boldsymbol{L}^p = \sum_{\alpha=1}^{n} \dot{\gamma}^{(\alpha)} \boldsymbol{s}^{(\alpha)} \otimes \boldsymbol{m}^{(\alpha)} . \quad (2)$$

where $\dot{\gamma}^{(\alpha)}$ is the slip rate on system α, and $\boldsymbol{s}^{(\alpha)}$ and $\boldsymbol{m}^{(\alpha)}$ denote the slip direction and slip plane normal, respectively, in the reference configuration. In crystal plasticity, it is assumed that slip does not affect crystal elasticity, and the elastic constitutive law can be described as [11]

$$\boldsymbol{\tau}^{\nabla^*} = \mathbb{C}: \boldsymbol{D}^*. \quad (3)$$

where $\boldsymbol{\tau}^{\nabla^*}$ is the Jaumann rate of elastic Kirchhoff stress, $\boldsymbol{D}^*$ is the elastic rate of deformation tensor, and $\mathbb{C}$ is the elastic stiffness tensor with tensor symmetry. To express the elastic response in the global frame, each grain's lattice orientation must be mapped from its local crystal coordinate system to the macroscopic reference frame. This coordinate transformation is performed using the rotation matrix $\boldsymbol{R}$. The elastic stiffness tensor in the sample frame is obtained as follows [12]:

$$\mathbb{C} = \boldsymbol{R}\mathbb{C}_{\boldsymbol{0}}\boldsymbol{R}^{\boldsymbol{T}}. \quad (4)$$

where coordinate rotation matrix R can be expressed in terms of transformation matrix T as follows

$$\boldsymbol{R} = \begin{bmatrix} (T_{11}^T)^2 & (T_{12}^T)^2 & (T_{13}^T)^2 & 2T_{11}^T T_{12}^T & 2T_{13}^T T_{11}^T & 2T_{12}^T T_{13}^T \\ (T_{21}^T)^2 & (T_{22}^T)^2 & (T_{23}^T)^2 & 2T_{21}^T T_{22}^T & 2T_{23}^T T_{21}^T & 2T_{22}^T T_{23}^T \\ (T_{31}^T)^2 & (T_{32}^T)^2 & (T_{33}^T)^2 & 2T_{31}^T T_{32}^T & 2T_{33}^T T_{31}^T & 2T_{32}^T T_{33}^T \\ T_{11}^T T_{21}^T & T_{12}^T T_{22}^T & T_{13}^T T_{23}^T & T_{11}^T T_{22}^T + T_{12}^T T_{21}^T & T_{13}^T T_{21}^T + T_{11}^T T_{23}^T & T_{12}^T T_{23}^T + T_{13}^T T_{22}^T \\ T_{31}^T T_{11}^T & T_{32}^T T_{12}^T & T_{33}^T T_{13}^T & T_{11}^T T_{32}^T + T_{12}^T T_{31}^T & T_{13}^T T_{31}^T + T_{11}^T T_{33}^T & T_{12}^T T_{33}^T + T_{13}^T T_{32}^T \\ T_{21}^T T_{31}^T & T_{22}^T T_{32}^T & T_{23}^T T_{33}^T & T_{22}^T T_{31}^T + T_{21}^T T_{32}^T & T_{21}^T T_{33}^T + T_{23}^T T_{31}^T & T_{22}^T T_{33}^T + T_{23}^T T_{32}^T \end{bmatrix}. \quad (5)$$

Here transformation matrix composed of Euler angles in Bunge's convention is as follows

$$\boldsymbol{T} = \begin{bmatrix} cos\phi_1 cos\phi_2 - sin\phi_1 sin\phi_2 cos\Phi & sin\phi_1 cos\phi_2 + cos\phi_1 sin\phi_2 cos\Phi & sin\phi_2 sin\Phi \\ -cos\phi_1 sin\phi_2 - sin\phi_1 cos\phi_2 cos\Phi & -sin\phi_1 sin\phi_2 + cos\phi_1 cos\phi_2 cos\Phi & cos\phi_2 sin\Phi \\ sin\phi_1 sin\Phi & -cos\phi_1 sin\Phi & cos\Phi \end{bmatrix}. \quad (6)$$

The critical resolved shear stress $\tau^{(\alpha)}$ on the slip system, α, can be expressed as follows

$$\tau^{(\alpha)} = \boldsymbol{m}^{*(\alpha)} \cdot \frac{\rho_0}{\rho} \boldsymbol{\tau} \cdot \boldsymbol{s}^{*(\alpha)}. \quad (7)$$

where $\boldsymbol{\tau}$ is the Kirchhoff stress tensor, ρ_0 and ρ are the mass densities in undeformed and deformed configurations, and $\boldsymbol{s}^{*(\alpha)}$ and $\boldsymbol{m}^{*(\alpha)}$ are the slip direction and the slip plane normal of system α,

respectively, in the deformed configuration. Rate-independent plasticity is the limiting form of a rate-dependent viscoplastic model [13]. In rate-sensitive crystals, the slip rate $\dot{\gamma}^{(\alpha)}$ depends on $\tau^{(\alpha)}$ as follows:

$$\dot{\gamma}^{(\alpha)} = \dot{\gamma}_0{}^{(\alpha)} \left(\frac{\tau^{(\alpha)}}{g^{(\alpha)}}\right) \left|\frac{\tau^{(\alpha)}}{g^{(\alpha)}}\right|^{\left(\frac{1}{m}\right)-1}. \tag{8}$$

where $\dot{\gamma}_0^{(\alpha)}$is the reference slip rate, $g^{(\alpha)}$the current slip resistance. The slip resistance incorporates lattice friction g_0, Voce-type hardening g_v, and Taylor hardening

$$g^{(\alpha)} = g_0 + g_v + Gb^{(\alpha)}\sqrt{\xi^2 \rho_{tot}}. \tag{9}$$

where G is shear modulus, $b^{(\alpha)}$ Burger's vector, ξ geometric factor, and ρ_{tot} total dislocation density. The total dislocation density, ρ_{tot}^{α}, is computed through projection operations that account for geometrically necessary dislocations (GNDs) of edge and screw types, with their respective line directions denoted as $\boldsymbol{n}_e^{(\beta)}$and $\boldsymbol{s}_s^{(\beta)}$[11]

$$\rho_{tot}^{\alpha} = \sum_{\beta} \left|\boldsymbol{m}^{(\alpha)} \cdot \boldsymbol{n}_e^{(\beta)}\right| \left|\rho_{GND,e}^{\beta}\right| + \left|\boldsymbol{m}^{(\alpha)} \cdot \boldsymbol{s}_s^{(\beta)}\right| \left|\rho_{GND,s}^{\beta}\right|. \tag{10}$$

Subscripts e and s denote the edge and screw components of the geometrically necessary dislocation density, respectively. Decomposition of the incompatibility tensor into edge, $\rho_{GND_e}^{(\alpha)}$, and screw, $\rho_{GND_s}^{(\alpha)}$, dislocation densities can be shown as follows

$$\boldsymbol{\Lambda} = \sum_{\alpha} \rho_{GND_e}^{(\alpha)} b^{(\alpha)} \boldsymbol{s}^{(\alpha)} \otimes \boldsymbol{n}^{(\alpha)} + \rho_{GND_s}^{(\alpha)} b^{(\alpha)} \boldsymbol{s}^{(\alpha)} \otimes \boldsymbol{s}^{(\alpha)}. \tag{11}$$

where $\boldsymbol{\Lambda}$ is the incompatibility tensor, $b^{(\alpha)}$ is the magnitude of the Burger vector and $\boldsymbol{n}^{(\alpha)}$ is the edge dislocation line direction [12, 14]:

$$\boldsymbol{\Lambda} = -(\boldsymbol{\nabla} \times \boldsymbol{F}^{p})^{T} \tag{12}$$

The constitutive behavior of each grain was introduced through a user-material subroutine (UMAT). The formulation implemented in this work is primarily based on the classical single-crystal plasticity model developed by Huang, a widely referenced framework in CPFEM studies [6]. Nevertheless, several numerical components were adapted from the Oxford UMAT implementation [12].

Throughout the simulations, Abaqus software is used for solving the constitutive updates. The constitutive updates within the UMAT rely on a forward-gradient (θ-method) time integration scheme. The slip activity $\dot{\gamma}^{(\alpha)}$ on a system α can be modeled as a function of the applied shear stress $\tau^{(\alpha)}$ and the present strength $g^{(\alpha)}$.

$$\Delta\gamma^{(\alpha)} = \Delta t \left[\dot{\gamma}_t^{(\alpha)} + \theta \frac{\partial \dot{\gamma}^{(\alpha)}}{\partial \tau^{(\alpha)}} \Delta\tau^{(\alpha)} + \theta \frac{\partial \dot{\gamma}^{(\alpha)}}{\partial g^{(\alpha)}} \Delta g^{(\alpha)}\right]. \tag{13}$$

Here $\dot{\gamma}_t^{(\alpha)}$describes the evaluated slipping rate at time t. θ represents the Euler time integration scheme. Hence, the increments of shear strain, $\Delta\gamma^{(\alpha)}$, can be obtained as follows

Representative polycrystalline geometries were constructed using Neper. The computational domain was defined as a cylindrical representative volume element (RVE) with a 1:1 height-to-diameter ratio. An example of created RVE is presented in Fig. 1.

Fig. 1. RVE created by Neper to be used in CPFEM simulation.

Crystallographic orientations were defined for each grain using Bunge Euler angles $(\varphi_1, \Phi, \varphi_2)$ within the crystal plasticity framework. For each grain, all twelve {111} <110> slip systems of the FCC crystal structure were evaluated, and the maximum Schmid factor among these systems was used as the primary indicator for slip system activity.

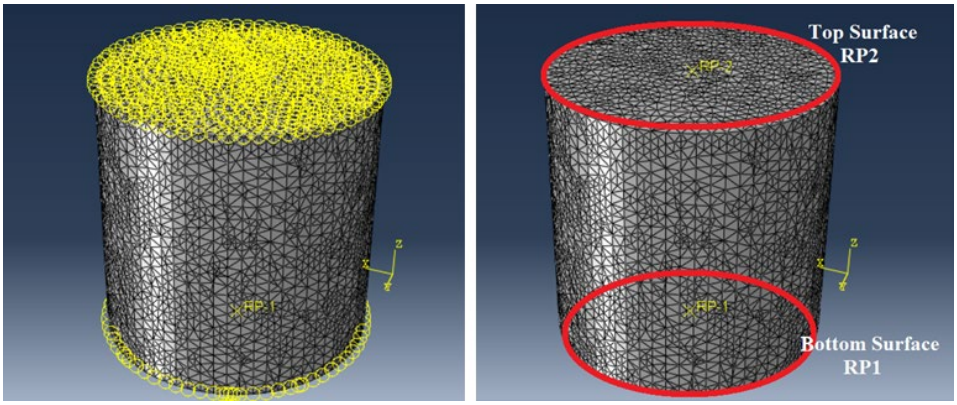

Fig. 2. Boundary conditions and related Reference Points (RP) are represented.

Polycrystalline geometries were meshed with C3D10 quadratic tetrahedral elements (four integration points) to capture strain gradients and rotation fields accurately. Mesh refinement was controlled through the Neper user defined dimensionless scaling factor which defines the characteristic element length, rcl, relative to the average grain size. Mesh length for each grain, cl, can be written as

$$cl = \frac{rcl}{l_{cell}} \tag{14}$$

where l_{cell} is the characteristic length of a grain. In Neper, the characteristic length of a grain is computed approximately in terms of its volume V_{cell} as $l_{cell} = (V_{cell})^{1/3}$.

Meshes were refined by adjusting cell volume to study resolution effects on deformation and stability. The top surface imposed 20% axial compression by applying an axial force (Fig. 2). Boundary conditions allowed free lateral strain, and frictionless contact was assumed to prevent barreling and isolate grain-scale plasticity as shown in Fig. 2.

The material parameters employed in this study are summarized in Table 1. All values were directly adopted from Demir et al. [12]. This reference provides a validated parameter set specifically calibrated for FCC copper, ensuring consistency with the crystal plasticity constitutive framework used in the present work.

Table 1. Selected Material Parameters of Cu for CPFEM.

Model Parameters	Value	Units
C_{11}	170	[GPa]
C_{12}	124	[GPa]
C_{44}	75	[GPa]
b	$2.56(10^{-4})$	[μm]
g_0	16	[MPa]
h_0	250	[MPa]
n	2.5	
q	1.4	

Results and Discussions

Grain Size Effects. Grain-size effects were studied using a single-crystal RVE and polycrystalline RVEs with 10, 100, and 500 grains, all under identical conditions. Models were generated in Neper with random seed placement to create unbiased 3D Voronoi tessellations, ensuring statistically uniform microstructures for reliable evaluation of grain-size influence (Fig. 3).

Grain orientations were randomly assigned to avoid texture bias, with mesh and boundary settings kept consistent with the baseline. After applying compressive load, the true stress -true strain curves were obtained. Stress–strain curves (Fig. 4) show clear grain-size strengthening; smaller grains (higher grain numbers) yield higher flow stress, while the single-grain model exhibits the lowest stress.

Table 2 summarizes flow stresses and stresses at 10% strain. As grain size decreases from single crystal to a RVE of 500 grains, yield stress rises from 41.86 MPa to 47.25 MPa, and stress at 10% strain from 125.0 MPa to 168.8 MPa. This corresponds to ~13% higher flow stress and ~35% higher strength, confirming classical grain-size strengthening due to increased grain-boundary density and GND accumulation [11].

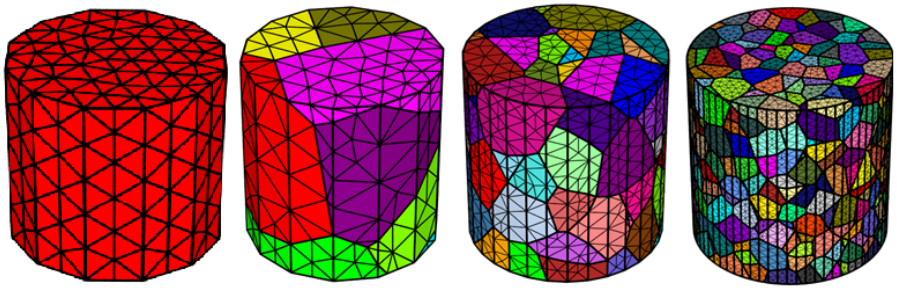

Fig. 3. RVE models for a single crystal and polycrystals with 10, 100, and 500 grains respectively.

To validate the grain-size dependence of the simulated flow stress, the results were fitted to the classical Hall–Petch relation:

$$\sigma_y = \sigma_0 + k_y d^{-1/2} \tag{15}$$

where k_y is the Hall-Petch constant, d is the average grain size, σ_y is the yield strength, and σ_0 is the lattice friction. For Hall–Petch validation, 0.2% offset method is used to determine the yield stresses ensuring consistent identification of plastic initiation across microstructures (Fig. 5).

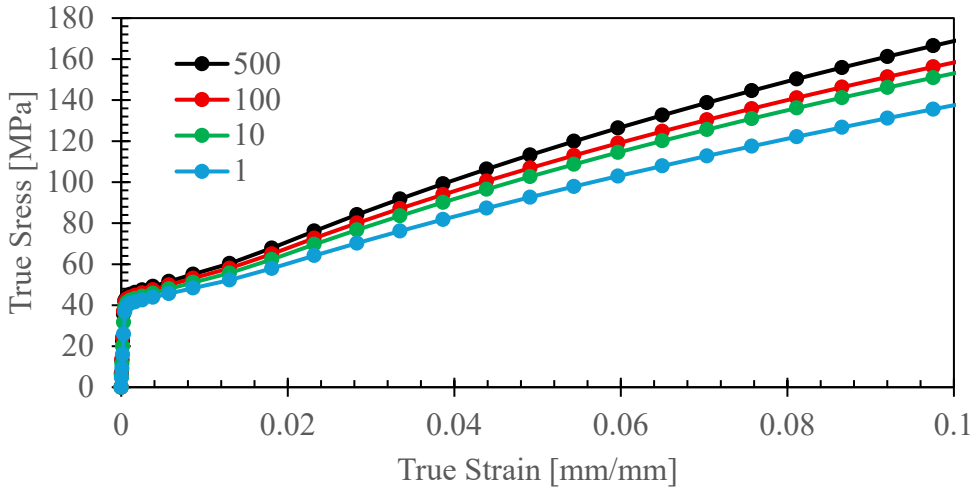

Fig. 4. True stress-strain curves for different grain numbers in RVE.

Table 2. Grain number, flow stresses and stress levels at 10% strain for different grain size.

Grain Number	Flow Stress [MPa]	Stress at 0.1 Strain [MPa]
500	47.25	168.79
100	45.52	158.37
10	44.06	153.04
Single crystal	41.86	125.00

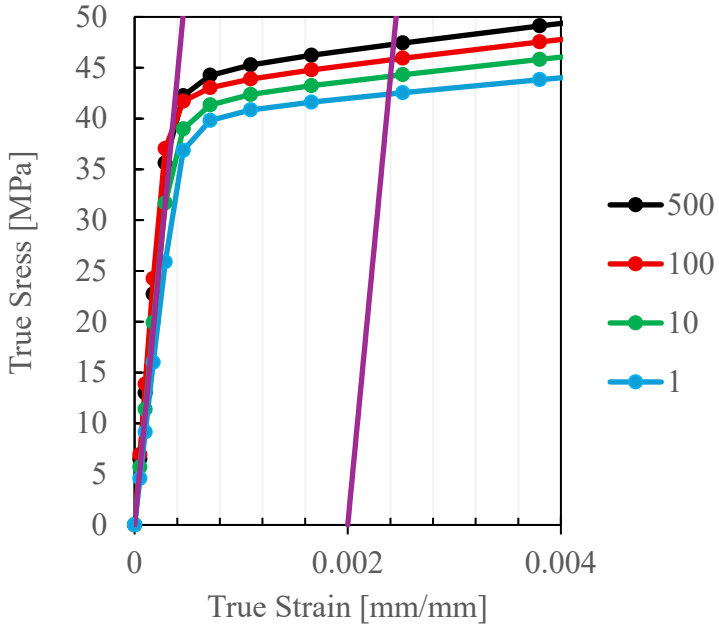

Fig. 5. Closer look at the 0.2% strain for different number of grains.

The corresponding plot of flow stress versus $d^{-1/2}$ exhibited a good linear correlation ($R^2 \approx 0.97$), confirming that the simulated data follow Hall–Petch scaling. The fitted parameters were found to be $\sigma_0 = 39.40$ MPa and $k_y = 120.79$ MPa $\cdot$ µm$^{1/2}$ and the related curves can be seen in the following Fig. 6. Results show good agreement with the experimentally reported values for pure copper presented by Cordero et al., who reported $\sigma_0 \approx 40$ MPa and $k_y \approx 110$ MPa $\cdot$ µm$^{1/2}$ [15].

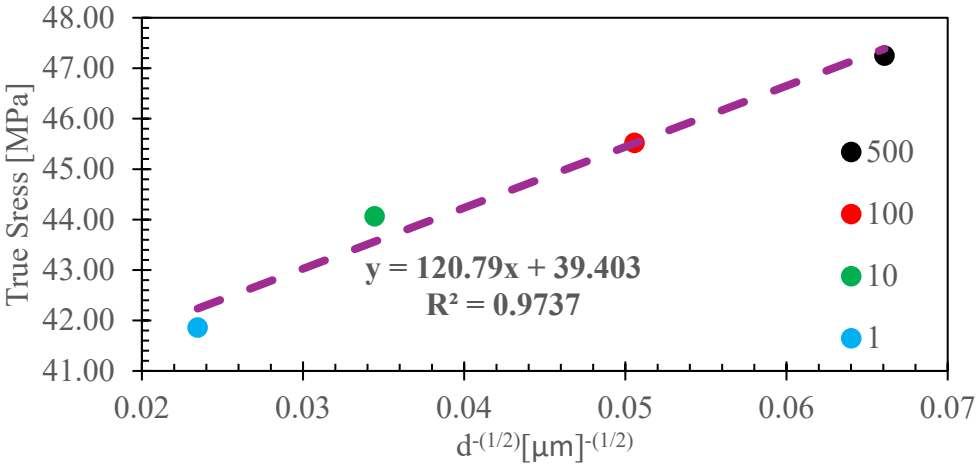

Fig. 6. Hall-Petch plot with curve fitting for $\sigma_y = \sigma_0 + k_y d^{-1/2}$.

Grain Orientation Effects on Single Crystal. To investigate the effect of grain orientation, two distinct sets of Euler angles are considered. The first orientation is arbitrarily defined by the Euler angles (0°, 45°, 45°). Schmid factor analysis (Table 3) indicates dominant activation of slip systems 4, 6, 7, and 8, with values ranging from 0.29 to 0.35, moderate activation of systems 2 and 3 (approximately 0.14), and negligible contributions from the remaining systems (<0.10). The maximum factor of 0.35 makes this orientation a suitable reference for studying crystallographic effects under uniaxial compression.

Accumulated slip (γ) for all twelve FCC systems under uniaxial compression shows dominant activity in systems 4, 6, 7, and 8, consistent with their high Schmid factors. Systems 2, 3, 11, and 12 exhibit moderate activation, while others remain largely inactive. This reflects the partially aligned slip character of the (0°, 45°, 45°) orientation, producing a plastic response governed by multiple active systems rather than a single mechanism. Fig. 7 illustrates this distribution, with intense slip in systems (d), (f), (g), and (h).

To identify the orientation with the lowest yield and flow stress, the Euler angles of the second set were chosen to maximize the Schmid factor (~0.5). This condition was met for (324°, 108°, 98°), where slip system 10 reached 0.49 (Table 3). Systems 4 and 10 show the highest Schmid factors among all slip systems.

Fig. 8 shows accumulated slip contours for the (324°, 108°, 98°) orientation, with activity concentrated in systems (d) and (j) which exhibit the most favorable geometric arrangement between the loading axis, the slip plane normal, and the slip direction. These systems accommodate most of the deformation, confirming this orientation corresponds to the lowest yield and flow stress among all cases.

Fig. 9 compares true stress–strain curves for (324°, 108°, 98°) and (0°, 45°, 45°) orientations. The latter, with a maximum Schmid factor of 0.35, shows higher flow stress and stronger hardening. At 20% strain, stresses are approximately 186 MPa and 260 MPa respectively, a difference of about 39.7% in plastic strength.

Table 3. Schmid factors for single crystal with two different Euler angles.

			Euler angles	
			0°, 45°, 45°	324°, 108°, 98°
Slip System	Slip Plane Normal	Slip Direction	Schmid Factor	Schmid Factor
1	(1,1,1)	[1, -1,0]	0.00	0.22
2	(1,1,1)	[0,1, -1]	0.14	0.04
3	(1,1,1)	[1,0, -1]	0.14	0.26
4	(-1,1,1)	[1,1,0]	0.29	0.46
5	(-1,1,1)	[0,1, -1]	0.06	0.10
6	(-1,1,1)	[1,0,1]	0.35	0.36
7	(1, -1,1)	[1,1,0]	0.29	0.25
8	(1, -1,1)	[0,1,1]	0.35	0.14
9	(1, -1,1)	[1,0, -1]	0.06	0.39
10	(1,1, -1)	[1, -1,0]	0.00	0.49
11	(1,1, -1)	[0,1,1]	0.14	0.20
12	(1,1, -1)	[1,0,1]	0.14	0.29

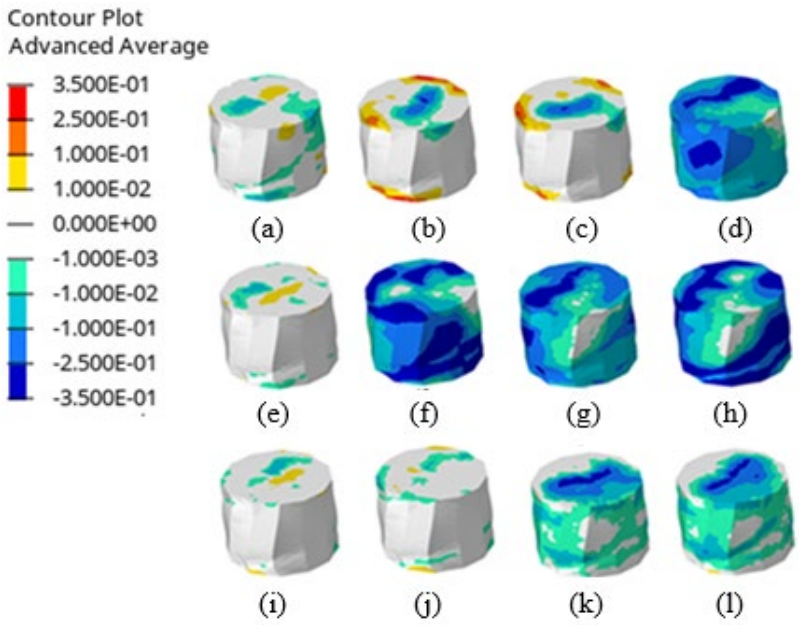

Fig. 7. For the single crystal with the Euler angles (0°, 45°, 45°), contours of the total accumulated slip (γ) on the twelve {111}⟨110⟩ slip systems: (a) 1, (b) 2, (c) 3, (d) 4, (e) 5, (f) 6, (g) 7, (h) 8, (i) 9, (j) 10, (k) 11, (l) 12.

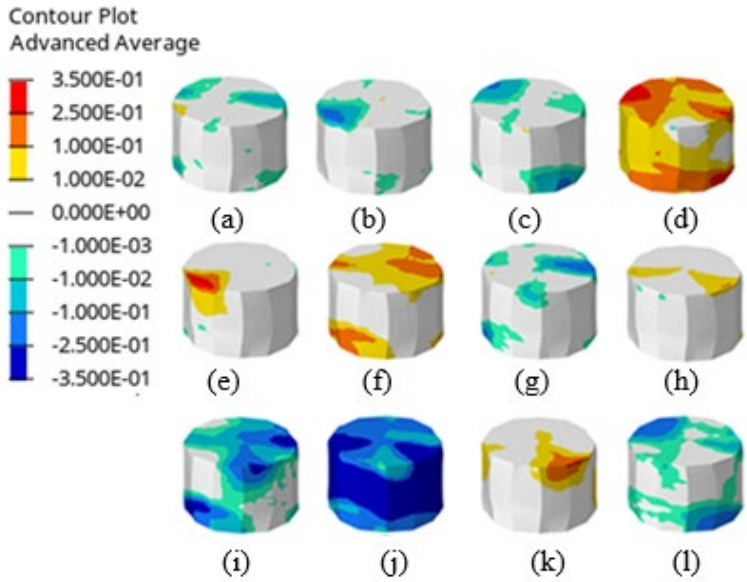

Fig. 8. For the single crystal with the Euler angles (324°, 108°, 98°) contours of the total accumulated slip (γ) on twelve {111}⟨110⟩ slip systems: (a) 1, (b) 2, (c) 3, (d) 4, (e) 5, (f) 6, (g) 7, (h) 8, (i) 9, (j) 10, (k) 11, (l) 12.

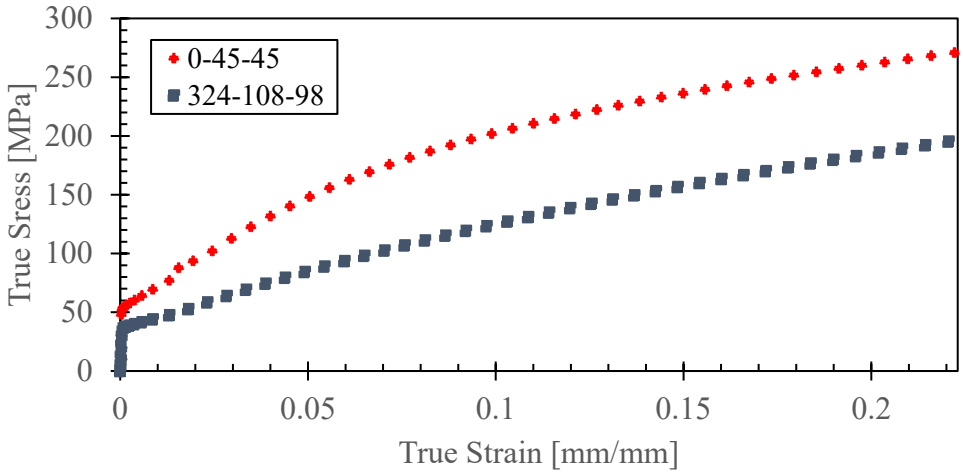

Fig.9. True stress-true strain comparison for single crystals with Euler angles of (0°, 45°, 45°) and (324°, 108°, 98°).

Comparison of Different Orientations for Single Crystal: To assess the effect of crystallographic alignment, the crystal was rotated from (0°, 45°, 45°) to (0°, 75°, 45°) in 5° increments. Table 4 shows that the maximum Schmid factor rises from 0.28 to 0.43, while true stress at 10% strain drops from 243.56 MPa to 147.41 MPa, confirming an inverse relation between slip alignment and flow strength. Fig. 10 illustrates this trend, with yield stress and hardening rate systematically decreasing as the Schmid factor increases.

Orientation Effects in Polycrystals. To investigate the effect of crystallographic orientation on the polycrystalline scale, RVEs with 500 grains were analyzed under identical boundary and loading conditions. For the 500-grain RVE, four orientations (324°, 108°, 98°), (0°, 45°, 45°), (0°, 55°, 45°), and (0°, 75°, 45°) were selected based on single-crystal results. To maintain these as mean values, $\pm 4^{o}$ deviation was applied to Φ and φ_2, while φ_1 remained fixed since rotation about the loading axis does not affect uniaxial response. This introduces realistic variability without making the RVE behave like a single crystal. Fig. 11 shows stress–strain curves, confirming the same trend: (324°, 108°, 98°) yields the lowest strength, (0°, 55°, 45°) the highest, and others fall in between. Table 5 summarizes stresses at 10% strain for direct comparison. Fig. 12 illustrates slip localization for (0°, 45°, 45°), with systems (d), (f), (g), and (h) most active, confirming multi-system slip behaviour.

Table 4. Max Schmid Factors for single crystals with different Euler Bunge angles.

Euler Angle	Max Schmid Factor	True Stress at %10 Strain [MPa]
0-55-45	0.28	243.56
0-50-45	0.31	226.92
0-60-45	0.33	209.96
0-45-45	0.35	202.66
0-65-45	0.37	179.56
0-70-45	0.41	158.43
0-75-45	0.43	147.41

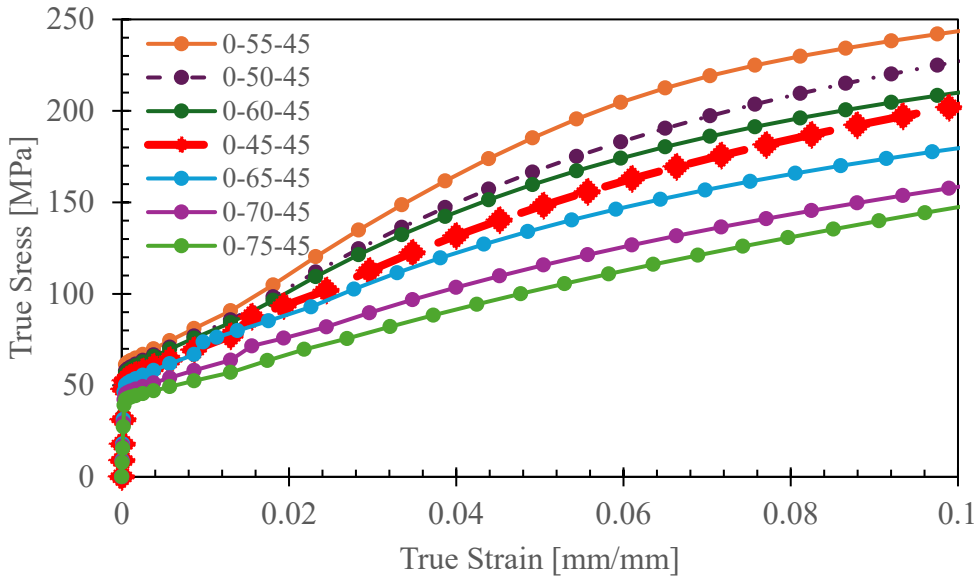

Fig. 10. True stress–true strain curves for single crystal at different orientations.

In the polycrystalline simulations, higher overall stress levels are observed compared to their single-crystal counterparts, reflecting the additional strengthening introduced by intergranular constraints and grain boundary interactions.

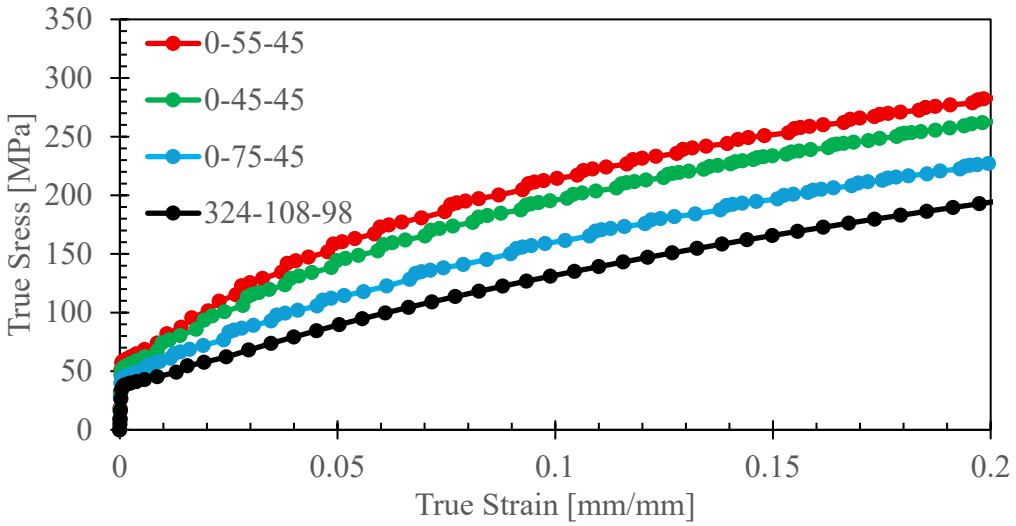

Fig. 11. True stress–true strain curves for a 500-grain polycrystal with different Euler angles.

Table 5. True stress-strain at 10% strain for different Euler Bunge Angles.

Euler Angle	Max Schmid Factor	True Stress at 10% Strain [MPa]
0-55-45	0.28	235.53
0-45-45	0.35	215.55
0-75-45	0.43	160.16
324-108-98	0.49	131.80

Coupled Effect of Orientation and Grain Size Variation. Two orientation distributions (Sets A and B) were generated around (324°, 108°, 98°), which corresponds to the orientation exhibiting the lowest stress among the selected cases. Using the same procedure as before, the Φ and φ_2 angles were varied with magnitudes of $\pm 10^o$ for Set A and $\pm 50^o$ for Set B while φ_1 was kept fixed. Welch's t-tests confirmed statistically significant differences (p-values $\ll 0.025$) between $\pm 10^o$ and $\pm 50^o$ cases; specifically, $p = 2.84(10^{-5})$ for 500 grains and $p = 0.0040$ for 50 grains.

Fig. 13 and Table 6 show that as the orientation variation increases from $\pm 10^o$ to $\pm 50^o$, the flow stress increases. For the 50-grain RVEs, the stress at 20% strain increases by 17.62 MPa (8.35%), whereas for the 500-grain RVEs the increase is 10.92 MPa (4.88%). Grain number moderates this effect: RVEs with fewer grains or larger grain sizes reflect orientation deviations more strongly, while RVEs with larger numbers of grains with smaller grain sizes tend to average them out.

A comparison between the 50-grain and 500-grain RVEs demonstrates that grain number and grain size control the macroscopic impact of orientation variation, as shown in Table 6. In the 50-grain RVEs, the smaller number of grains and their larger size limit averaging, so the stress reflects orientation deviations more directly. In contrast, in the 500-grain RVEs, the larger number of smaller grains increases averaging, reducing the sensitivity to orientation variation. This is evident in the reduction of the stress variation from 8.35% to 4.88%.

Overall, the $\pm 10^o$ versus $\pm 50^o$comparison confirms that orientation variation affects the aggregate response, and that its impact depends strongly on the number of grains within the RVE.

Table 6. Comparative analysis of 50 and 500 Grains for $\pm 10^o$ and $\pm 50^o$ standard deviations.

	50 Grain		500 Grain	
Set	$\sigma = 10$	$\sigma = 50$	$\sigma = 10$	$\sigma = 50$
Stress at %20 Strain [MPa]	210.93	228.55	223.84	234.76
Difference [MPa]	17.62		10.92	
Variation [%]	8.35		4.88	

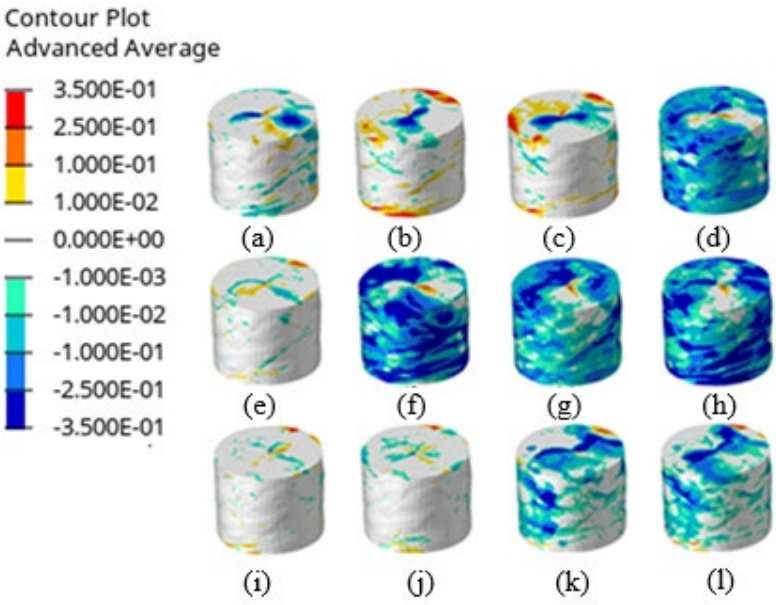

Fig. 12. For the Euler angles (0°, 45°, 45°) contours of the total accumulated slip (γ) for the twelve {111}⟨110⟩ slip systems in 500 grain polycrystal: (a) 1, (b) 2, (c) 3, (d) 4, (e) 5, (f) 6, (g) 7, (h) 8, (i) 9, (j) 10, (k) 11, (l) 12.

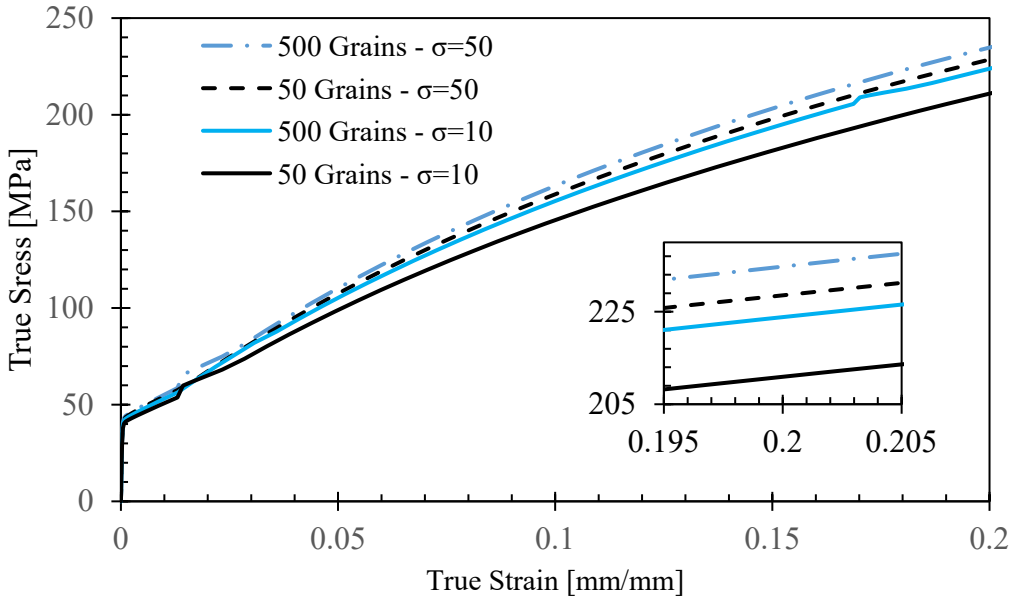

Fig.13. True stress–true strain curves for $\pm 10^{o}$ versus $\pm 50^{o}$ variations.

Conclusions

The combined findings elucidate the governing mechanisms in crystal plasticity:

1. Orientation alignment dictates local slip activity and controls the onset and nature of hardening.
2. Polycrystalline interactions increase overall material strength.
3. Grain size reduction increases yield stress and flow strength in accordance with Hall–Petch scaling.
4. Orientation variation and neighborhood constraints govern the transition from local anisotropy to global homogeneity.

In conclusion, the mechanical response of polycrystalline copper is shown to arise from a delicate balance between crystallographic anisotropy and intergranular compatibility. The present CPFEM framework provides a numerically stable and physically consistent basis for analyzing texture effects, hardening behavior, and strain localization in FCC materials.

References

[1] P. Wang, L. Ma, X. Cheng, and X. Li, “Effect of grain size and crystallographic orientation on the corrosion behaviors of low alloy steel,” Journal of Alloys and Compounds, vol. 857, 158258, 2021; https://doi.org/10.1016/j.jallcom.2020.158258

[2] A. Bahmani, S. Moradi, M. Lotfpour, H. T. Jeong, and W. J. Kim, “Effect of grain size on the corrosion resistance of the Fe41Mn25Ni24Co8Cr2 high entropy alloy,” Corrosion Science, vol. 230, 111892, 2024; https://doi.org/10.1016/j.corsci.2024.111892

[3] R. Hill, Continuum micro-mechanics of elastoplastic polycrystals, Journal of the Mechanics and Physics of Solids, vol.13, 1965,pp.89-101, https://doi.org/10.1016/0022-5096(65)90023-2.

[4] R. J. Asaro and J. R. Rice, “Strain localization in ductile single crystals,” Journal of the Mechanics and Physics of Solids, vol. 25, no. 5, pp. 309–338, 1977, https://doi.org/10.1016/0022-5096(77)90001-1

[5] R. J. Asaro, “Micromechanics of crystals and polycrystals,” Advances in Applied Mechanics, vol. 23, pp. 1–115, 1983; https://doi.org/10.1016/S0065-2156(08)70242-4

[6] Y. Huang, A User-Material Subroutine Incorporating Single Crystal Plasticity in the ABAQUS Finite Element Program. Cambridge, MA: Harvard University, 1991, pp. 1–21

[7] J. F. Nye, “Some geometrical relations in dislocated crystals,” Acta Metallurgica, vol. 1, no. 2, pp. 153–162, 1953 https://doi.org/10.1016/0001-6160(53)90054-6

[8] A. Vattré, “HDR: Interfaces in crystalline materials,” arXiv preprint arXiv:2307.14569, pp. 40–50, 2023; https://arxiv.org/abs/2307.14569

[9] Raabe, D., Zhao, Z., Park, S. J., and Roters, F. (2002). Theory of orientation gradients in plastically deformed crystals. Acta Materialia, 50, 421–440.

[10] A. Arsenlis, D. M. Parks, R. Becker, and V. V. Bulatov, “On the evolution of crystallographic dislocation density in non-homogeneously deforming crystals,” Journal of the Mechanics and Physics of Solids, vol. 52, no. 6, pp. 1213–1246, 2004; https://doi.org/10.1016/j.jmps.2003.12.007

[11] R. Hill and J. R. Rice, “Constitutive analysis of elastic–plastic crystals at arbitrary strain,” Journal of the Mechanics and Physics of Solids, vol. 20, no. 6, pp. 401–413, 1972; https://doi.org/10.1016/0022-5096(72)90017-8

[12] E. Demir, A. M. Pecchero, C. Hardie, and E. Tarleton, “OXFORD-UMAT: An efficient and versatile crystal plasticity framework International Journal of Solids and Structures, vol. 307, 2025, https://doi.org/10.1016/j.ijsolstr.2024.113110

[13] D. Peirce, R. I. Asaro, and A. Needleman, “Material rate dependence and localized deformation in crystalline solids,” Acta Metallurgica, vol. 31, no. 12, pp. 1951–1976, 1983; https://doi.org/10.1016/0001-6160(83)90014-7

[14] S. Das, A. Tarleton, and E. Tarleton, “Consistent determination of geometrically necessary dislocation density from simulations and experiments,” International Journal of Plasticity, vol. 109, pp. 18–42, 2018; https://doi.org/10.1016/j.ijplas.2018.05.001

[15] Z.C. Cordero, B.E. Knight, and C.A. Schuh, “Six decades of the Hall–Petch effect – a survey of grain-size strengthening studies on pure metals,” International Materials Reviews, vol. 61, pp. 495-512, 2016; https://doi.org/10.1080/09506608.2016.1191808.